# Electronic supplementary information

## Well-designed internal electric field from nano-ferroelectrics promote formic acid oxidation on Pd

*Guoming Luo [†], Shuozhen Hu [†,*], Dongfang Niu [†], Shigang Sun [‡], Xinsheng Zhang [†,**]*

*[†]State Key Laboratory of Chemical Engineering, School of Chemical Engineering, East China University of Science and Technology, Shanghai 200237, China.*

*[‡]State Key Laboratory of Physical Chemistry of Solid Surfaces, College of Chemistry and Chemical Engineering, Xiamen University, Xiamen, China*

**Contents**

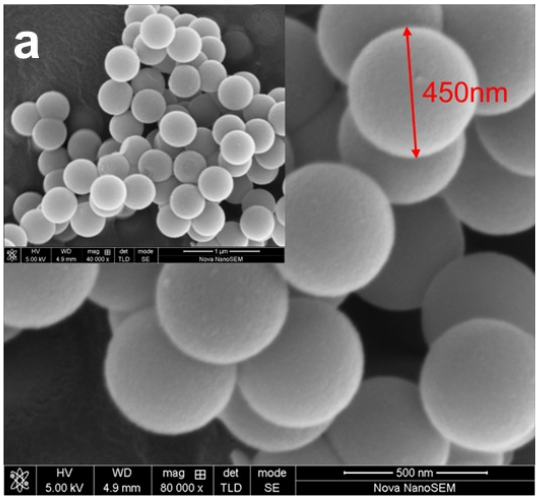


**Fig. S1** SEM images of RFC.

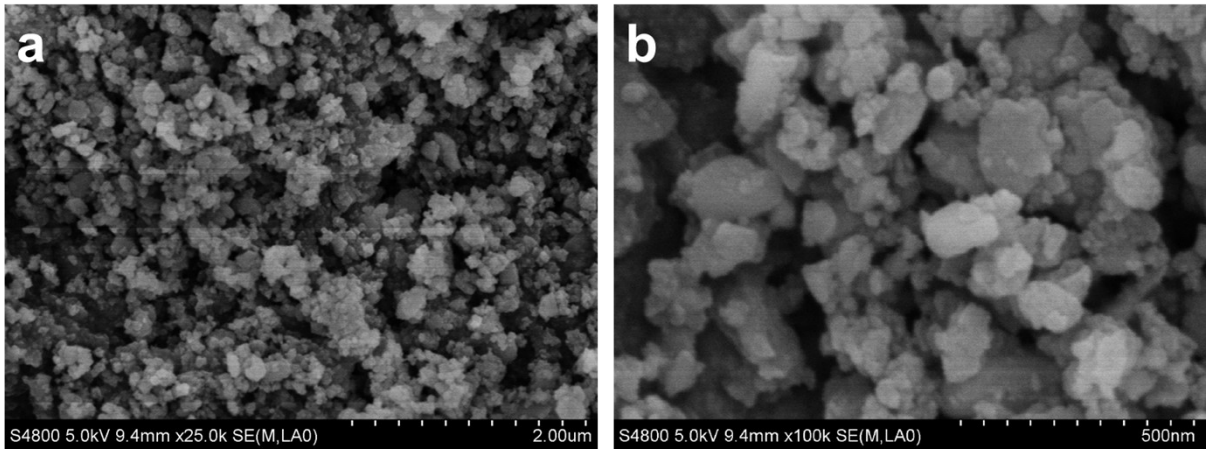


**Fig. S2** SEM images of TNP.

**Fig. S3** SEM images of $TNP_{6.67}$@RFC@$Pd_1$.

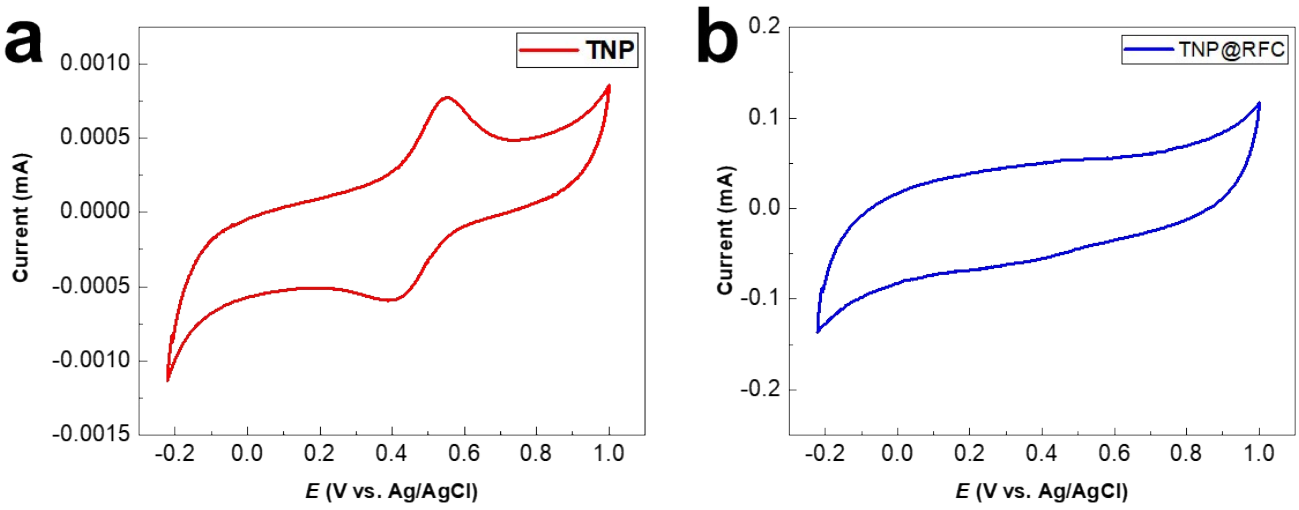


**Fig. S4** CVs of (a) TNP and (b) TNP@RFC in 0.5 M $H_2SO_4$ with a scanning rate of 50 mV $s^{-1}$.

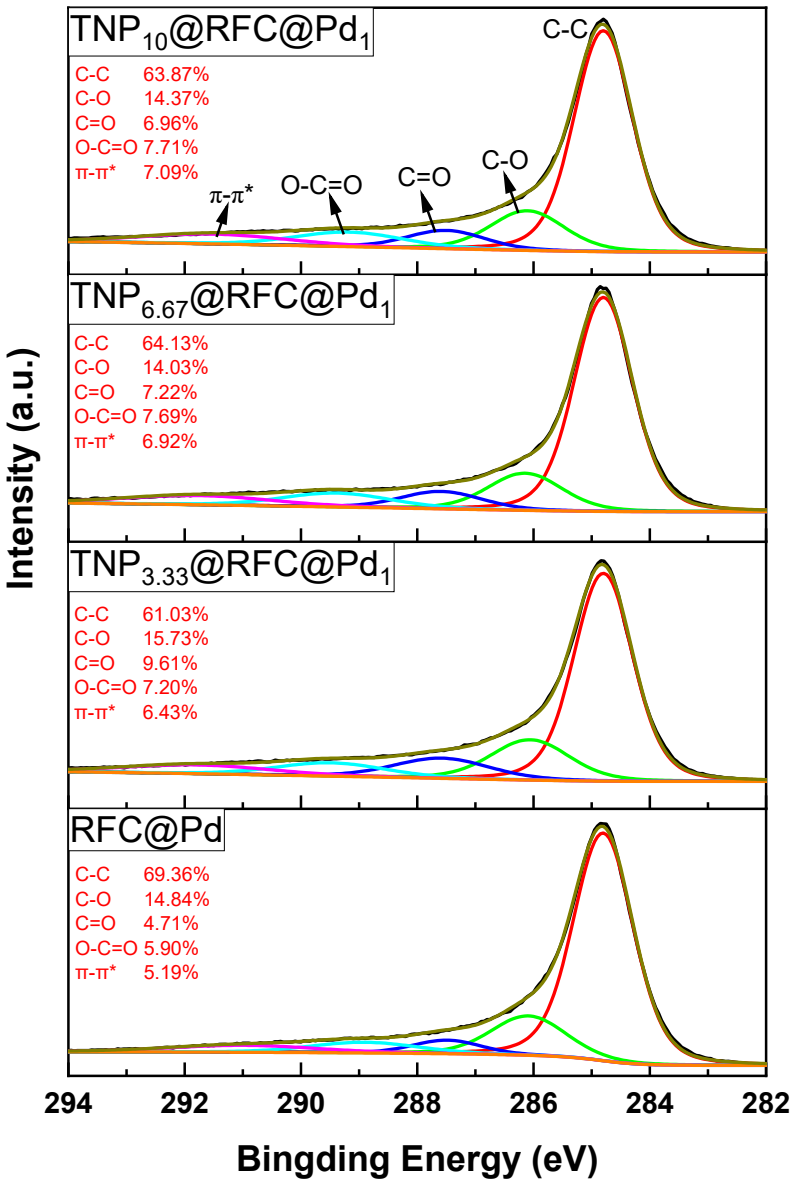


**Fig. S5** XPS core-level binding energy of C 1s of all catalysts.

Since resin is a type of carbohydrate material, a variety of oxygen-containing functional groups, such as-OH, C-O-C, -COOH, or C=O groups, exists in the polymerized-resin coating layer before the carbonization. During the carbonization, the oxygen-containing functional groups were decomposed. As the XPS spectra show (Fig. S5), the C 1s XPS spectra are deconvoluted into five peaks, which are assigned to C-C at about 284.8 eV for carbon groups, the C-O groups at about 286.1 eV for hydroxyl groups or ethers, C=O groups at about 287.5 eV for carbonyl or quinone groups, O-C=O groups at about 289.3 eV for carboxylic groups, esters or lactones, and π-π* groups at about 291.6 eV. Detailed component content is listed in Fig. S5. The sp2 hybridized carbon is the majority and the surface composition of the carbon layer for all the TNP@RFC@Pd and RFC@Pd catalysts are about the same to each other. Such a result indicates that the addition of tourmaline has an

insignificant effect on the surface composition of the carbon layer. Thus, the electronic structure change and the electrochemical performance difference of the as-synthesized Pd-based catalysts result from tourmaline, not the carbon layer.

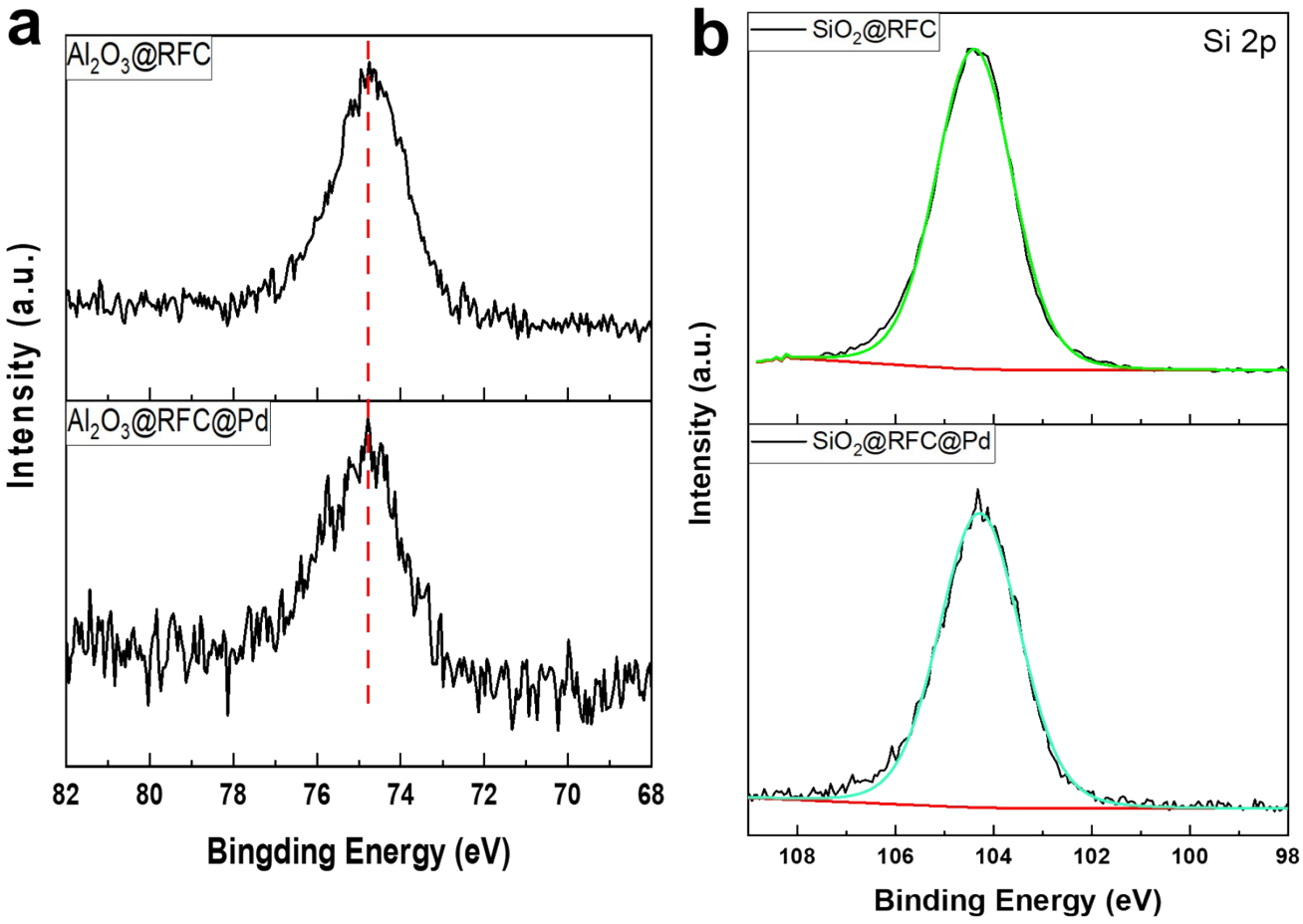


**Fig. S6** XPS core-level spectra of (a) Al 2p of $Al_2O_3$@RFC and $Al_2O_3$@RFC@Pd, and (b) Si 2p of $SiO_2$@RFC and $SiO_2$@RFC@Pd.

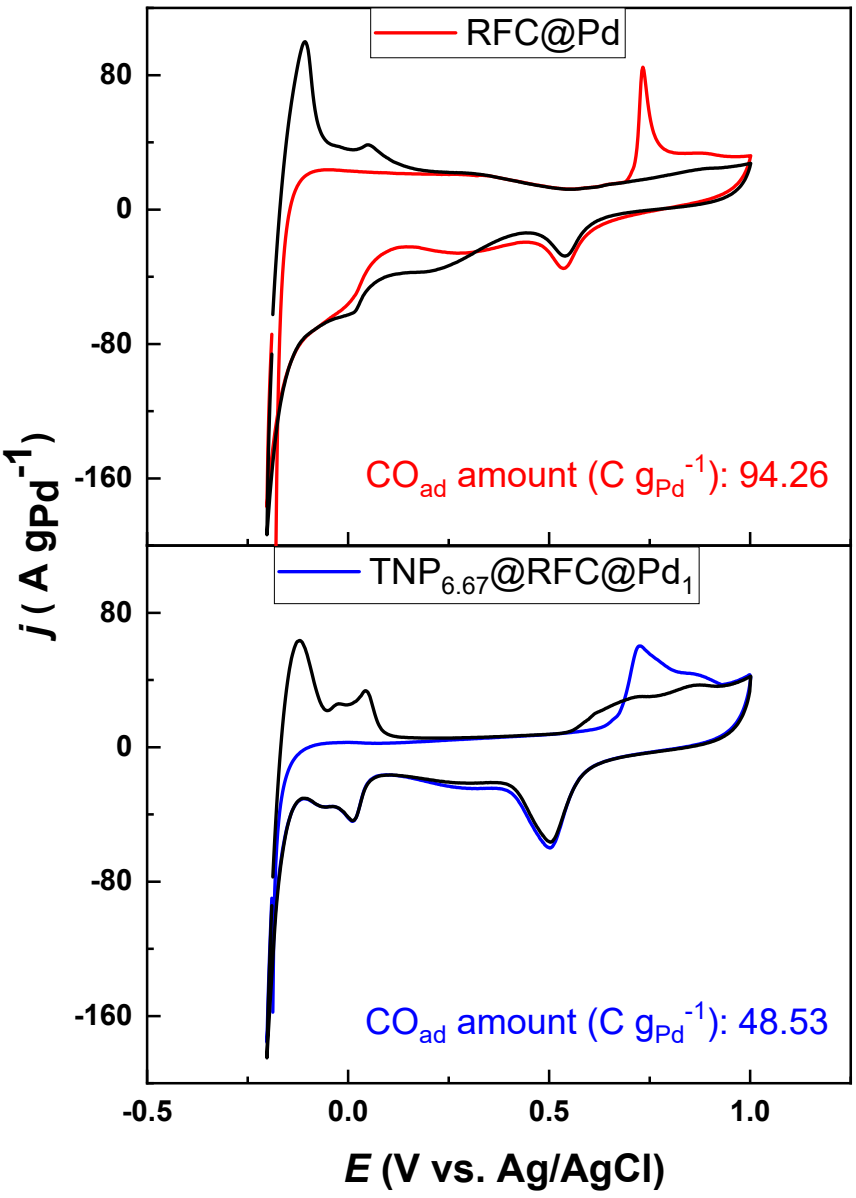


**Fig. S7** CO stripping(CA) results of RFC@Pd and $TNP_{6.67}$@RFC@$Pd_1$ in 0.5 M $H_2SO_4$ electrolyte.

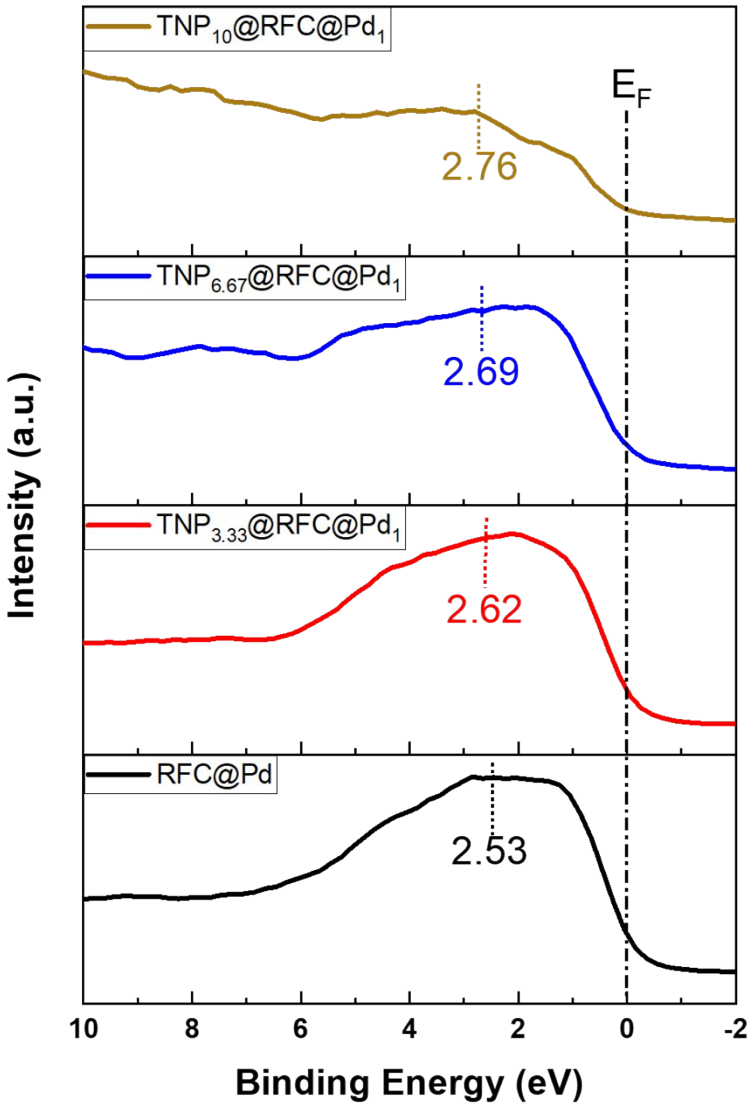


**Fig. S8** XPS Valence band spectra of RFC@Pd, $TNP_{3.33}$@RFC@$Pd_1$, $TNP_{6.67}$@RFC@$Pd_1$, and $TNP_{10}$@RFC@$Pd_1$ catalysts.

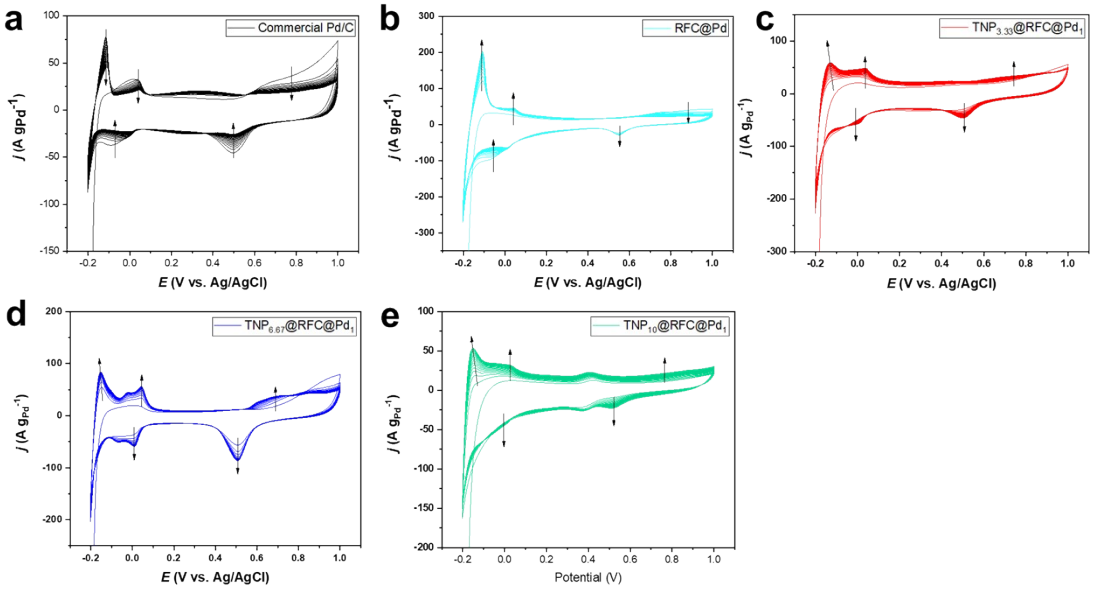


**Fig. S9** CV of (a) commercial Pd/C, (b) RFC@Pd, (c) $TNP_{3.33}$@RFC@$Pd_1$, (d) $TNP_{6.67}$@RFC@$Pd_1$, and (e) $TNP_{10}$@RFC@$Pd_1$ in 0.5 M $H_2SO_4$ with a scanning rate of 50 mV $s^{-1}$ for 20 cycles.

As Fig. S9 shows, the CV cycling variation of the commercial Pd/C is different from those of RFC@Pd and TNP@RFC@Pd catalysts. The peak current of all the typical CV features for commercial Pd/C is gradually decreased, meaning that Pd is lost during the CV measurements. The loss of Pd is mainly due to the partial electro-dissolution of Pd at potentials higher than 0.8 V vs Ag/AgCl (sat. KCl). Conversely, the current density of such peaks for RFC@Pd and TNP@RFC@Pd catalysts consistently increase and become stable after 20 cycles. It can be seen that the Pd in commercial Pd/C has poor survival conditions and cannot adapt to the activation of 20 circles CV. Therefore, we finally take only five cycles of CV measurements to activate the commercial Pd/C and to calculate ECSA, during which the structure of commercial Pd/C should not be significantly changed. Therefore, the dissolving of Pd could be ignored. The increase of peak current densities, especially for $TNP_{6.67}$@RFC@$Pd_1$, is due to the carbon layer coated over Pd NPs. Fresh Pd surfaces are created by the slight removal of the carbon layer during CV measurements. Moreover, due to the unique partially embedded structure of Pd NPs in RFC and the carbon coating layer over Pd, the current densities of all the peaks for RFC@Pd and TNP@RFC@Pd catalysts becomes stable without noticeable decrease after 20 cycles of CV measurement. Thus, the electro-dissolution of Pd is prevented.

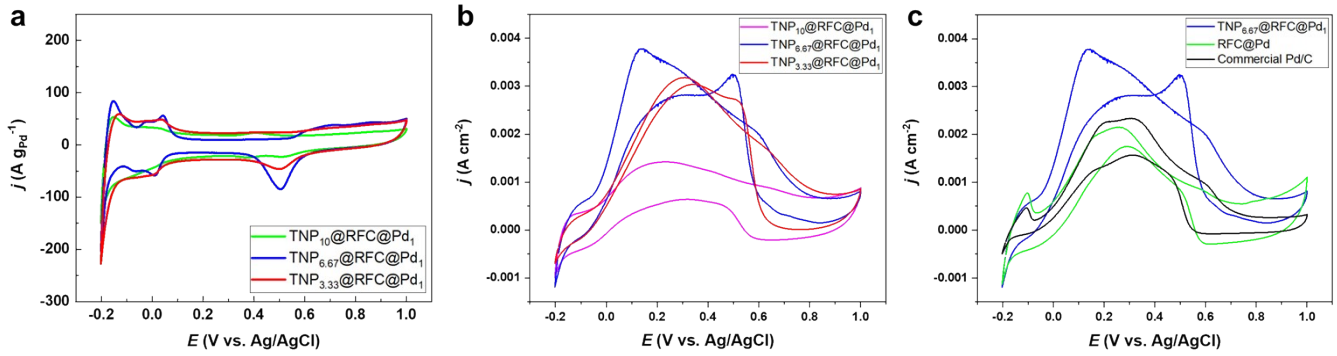


**Fig. S10** CV results of TNP@RFC@Pd catalysts in (a) 0.5 M $H_2SO_4$ and (b) 0.5 M $H_2SO_4$ and 0.5 M HCOOH electrolyte at a scan rate of 50 mV $s^{-1}$. (c) CV results of $TNP_{6.67}$@RFC@$Pd_1$, RFC@Pd, and commercial Pd/C catalysts in 0.5 M $H_2SO_4$ and 0.5 M HCOOH electrolyte.

**Table S1** The conductivity of deionized water treated by Pd-based catalysts.

| Samples | Ionic conductivity of deionized water treated by catalysts[a] ($\mu s\ cm^{-1}$) | | |
|---|---|---|---|
| | before filtration | | after filtration |
| | 30 min | 2 h | 1h |
| Commercial Pd/C | 2.02 ± 0.01 | 2.02 ± 0.01 | 2.03 ± 0.01 |
| RFC@Pd | 2.02 ± 0.01 | 2.02 ± 0.01 | 2.04 ± 0.01 |
| $TNP_{3.33}$@RFC@$Pd_1$ | 4.23 ± 0.01 | 6.39 ± 0.02 | 3.41 ± 0.01 |
| $TNP_{6.67}$@RFC@$Pd_1$ | 5.58 ± 0.02 | 8.52 ± 0.02 | 4.08 ± 0.01 |
| $TNP_{10}$@RFC@$Pd_1$ | 7.61 ± 0.02 | 12.46 ± 0.02 | 4.79 ± 0.02 |

[a] The ionic conductivity of untreated deionized water is 1.98 ± 0.01 $\mu s\ cm^{-1}$.

**Table S2** Concentrations of metal ions in the filtered water treated by TNP and TNP@RFC, respectively.

| Samples | Concentrations of metal ions ($\mu g\ mL^{-1}$) | | | | |
|---|---|---|---|---|---|
| | $Al^{3+}$ | $Mg^{2+}$ | $Fe^{3+}$ | $Ca^{2+}$ | $Na^{+}$ |
| Pure $H_2O$ | 0.008 | 0.009 | 0.005 | 0.004 | 0.010 |
| TNP-treated $H_2O$ | 4.881 | 0.124 | 0.230 | 0.072 | 0.055 |
| TNP@RFC-treated $H_2O$ | 0.356 | 0.019 | 0.010 | 0.004 | 0.013 |

Five catalysts were added to 20 mL DI water, stirred, and dispersed evenly. The ionic conductivity of corresponding treated DI water was measured at 30 min and 2 h. Then, these five solutions were filtered to remove the catalysts, and the conductivity of the filtrates was measured again after standing for 1 h. The results are shown in Table S1. For commercial Pd/C and RFC@Pd treated DI water, the ionic conductivity is not changed. However, when the DI water is treated by TNPs contained catalysts, the ionic conductivity increases. Moreover, the conductivity of DI water increases as the amount of TNPs in TNP@RFC@Pd increases. Thus, the ionic conductivity increase of DI water is caused by the TNPs.

Since tourmaline is a mineral with a strong spontaneous polarized electric field, water can be dissociated into $H^+$ and $OH^-$. Water dissociation is one of the reasons that increase the ionic conductivity of DI water. However, tourmaline is a natural borosilicate mineral with the formula of $XY_3Z_6Si_6O_{18}(BO_3)_3W_4$, where X is $Na^+$, $Ca^{2+}$, $K^+$, or vacancy, Y is $Mg^{2+}$, $Fe^{2+}$, or $Mn^{2+}$, Z is $Al^{3+}$, $V^{3+}$, or $Cr^{3+}$, and W is $OH^-$, $F^-$, or $O^{2-}$ [1-2]. The metal ions in tourmaline could be replaced by $H^+$ ions from water and remain in the water. Consequently, the increase of ionic conductivity of DI water could also result from the ion exchange. Hence, the absence of ion exchange phenomena has to be proved to utilize the ionic conductivity of DI water to represent the water dissociation and polarized-electric field strength. As Table S1 shows, after the catalyst is filtered, the conductivity of DI water greatly decreases. If there is a large number of ions exchanged, the ionic conductivity of DI water should be remained high after

removing TNP@RFC@Pd. However, this did not happen. Even though the ionic conductivity of TNP@RFC@Pd-treated DI water is higher after removing TNP@RFC@Pd catalysts, which is probably caused by the small amount of ion exchange, the increase of ionic conductivity with the presence of TNP@RFC@Pd is much higher than that after the removal of TNP@RFC@Pd. Thus, the carbon layer over TNPs could suppress the ion-exchange phenomenon. Water dissociation is the main reason that causes the increase of ionic conductivity of DI water.

To further demonstrate the increase of ionic conductivity of DI water with the presence of tourmaline is due to the polarized-electric field, instead of ion-exchange, ICP-MS of the DI water after removing TNPs and TNP@RFC is measured to detect the concentration of metal ions and added as Table S2 in the supplementary material. The results show that the concentration of metal ions in the TNP@RFC-treated DI water increases compared to pure DI water. However, the amount of metal ions is dramatically lower than that in TNPs-treated DI water. Therefore, the carbon layer could significantly prevent ion exchange on the tourmaline surface. Namely, the ionic conductivity of DI water could represent the water dissociation ability and strength of polarized electric-field of TNP@RFC@Pd catalysts.

In addition, CV tests were conducted in 0.5 mol $L^{-1}$ $H_2SO_4$. As Fig. S4a shows, distinct anodic and cathodic peaks are detected for TNP, which is possibly from the release and re-adsorption of metal ions on the tourmaline surface. However, such peaks disappear for TNP@RFC and a typical carbon CV feature is detected (shown in Fig. S4b) after coating the carbon layer over tourmaline. Thus, the carbon layer could prevent metal ions release from tourmaline into solution resulting in good acid resistance and improved conductivity of TNP@RFC in the acid system.

**Table S3** Physical characteristics of catalysts.

| Samples | Pd (111) at 2θ (◦) | Lattice parameter d[a] (Å) | d (111) by TEM (Å) | Crystal lite size $\tau$[b] (nm) | Particle size by TEM (nm) |
|---|---|---|---|---|---|
| RFC@Pd | 40.127 | 2.334 | 2.33 | 8.84 | 7.45 |
| $TNP_{3.33}$@RFC@$Pd_1$ | 40.209 | 2.297 | 2.29 | 7.62 | 6.69 |
| $TNP_{6.67}$@RFC@$Pd_1$ | 40.270 | 2.238 | 2.24 | 5.81 | 4.19 |
| $TNP_{10}$@RFC@$Pd_1$ | 40.533 | 2.165 | 2.17 | 8.59 | 8.03 |

[a] d is calculated by Bragg's law. $2d\sin\theta = n\lambda$, where n is an integer, λ is the wavelength of the incident wave, d is the spacing between the planes in the atomic lattice, and θ is the angle between the incident X-ray and the scattering planes.

[b] $\tau$ is calculated by Scherrer equation: $\tau = \frac{K\lambda}{\beta cos\theta}$, where $\tau$ is the mean size of the ordered (crystalline) domains. K is a dimensionless shape factor, with a typical value of about 0.89. $\lambda$ is the X-ray wavelength. β is the full width at half maximum intensity (FWHM), after subtracting the instrumental full width, in radians. $\theta$ is the Bragg angle.

**Table S4** The mass percentage of Pd in all catalysts obtained from ICP-AES-MS.

| Samples | Mass percentage (%) |
|---|---|
| Commercial Pd/C | 10.0 |
| RFC@Pd | 13.0 |
| $TNP_{3.33}$@RFC@$Pd_1$ | 10.8 |
| $TNP_{6.67}$@RFC@$Pd_1$ | 9.0 |
| $TNP_{10}$@RFC@$Pd_1$ | 7.9 |

**Table S5** Summary of the electrocatalytic performance of reported Pd-based catalysts toward FAO.

| | | Catalysts | Mass Activity ($A\ g^{-1}$) [a] | Condition | Scan rate ($mV\ s^{-1}$) | Year | Ref. |
|---|---|---|---|---|---|---|---|
| 1 | Single-Pd nanocatalyst | Pd nanoparticles on DNA-Graphene | 140 | 0.5 M $H_2SO_4$ + 0.5 M HCOOH | 50 | 2013 | 3 |
| 2 | | Pd nanosheet | 630 | 0.1 M $HClO_4$ + 0.2 M HCOOH | 50 | 2015 | 4 |
| 3 | | Pd nanowires | 758.0 | 0.5 M $H_2SO_4$ + 0.5 M HCOOH | 50 | 2016 | 5 |
| 4 | | Pd/NS-G | 501.8 | 0.5 M $H_2SO_4$ + 0.5 M HCOOH | 50 | 2016 | 6 |
| 5 | | Pd/NP-Coal-CFs (DCD/TPP) | 536.6 | 0.5 M $H_2SO_4$ + 0.5 M HCOOH | 50 | 2019 | 7 |
| 6 | | PdNCs/fG | 494.5 | 0.5 M $H_2SO_4$ + 2.0 M HCOOH | 50 | 2019 | 8 |
| 7 | | $Pd/(C_{16}mim)_3PMo_{12}O_{40}$/NP-CFs | 754.1 | 0.5 M $H_2SO_4$ + 0.5 M HCOOH | 50 | 2020 | 9 |
| 8 | | $TNP_{6.67}$@RFC@$Pd_1$ | 905 | 0.5 M $H_2SO_4$ + 0.5 M HCOOH | 50 | - | This work |
| 9 | Pd-based alloy/core-shell nanocatalyst | Pd-Co nanoparticle | 770 | 0.1 M $HClO_4$ + 0.2 M HCOOH | 50 | 2012 | 10 |
| 10 | | $Pd_1Ni_1$/NG | 709 | 0.5 M $H_2SO_4$ + 1 M HCOOH | 20 | 2016 | 11 |
| 11 | | $Au_{71}$@$Pd_{29}$ DCS | 1405 | 0.5 M $H_2SO_4$ + 0.5 M HCOOH | 50 | 2020 | 12 |
| 12 | | Ru@Pd/C | 530 | 0.5 M $H_2SO_4$ + 0.5 M HCOOH | 50 | 2017 | 13 |

[a] Normalized to the weight of Pd.

**Table S6** Fitting results of electrochemical impedance spectroscopy (EIS) for RFC@Pd, $TNP_{3.33}$@RFC@$Pd_1$, $TNP_{6.67}$@RFC@$Pd_1$, and $TNP_{10}$@RFC@$Pd_1$.

| Samples | $R_S$ ($\Omega$ $cm^2$) | $R_{CT}$ ($\Omega$ $cm^2$) | CPE (S $s^{-n}$ $cm^2$) | n (0<n<1) |
|---|---|---|---|---|
| Commercial Pd/C | 1.42 | 146.37 | 8.49E-4 | 0.993 |
| RFC@Pd | 1.17 | 8.40 | 5.27E-4 | 0.982 |
| $TNP_{3.33}$@RFC@$Pd_1$ | 1.16 | 9.97 | 2.36E-5 | 0.911 |
| $TNP_{6.67}$@RFC@$Pd_1$ | 1.18 | 10.42 | 8.16E-5 | 0.917 |
| $TNP_{10}$@RFC@$Pd_1$ | 1.37 | 54.91 | 1.75E-4 | 0.889 |

$R_S$ is a signal of uncompensated solution resistance, $R_{CT}$ represents the charge transfer resistance at the electrolyte-catalyst interface, and the constant phase element (CPE) represent a double-layer capacitor.

**Table S7** The dissolution amount of Pd from $TNP_{6.67}$@RFC@$Pd_1$, RFC@Pd, and commercial Pd/C catalysts after the accelerated durability test.

| Catalysts | Content (ppb) |
|---|---|
| $TNP_{6.67}$@RFC@$Pd_1$ | 12.4 |
| RFC@Pd | 15.2 |
| Commercial Pd/C | 83.7 |

**Reference**

(1) Zhu, D.; Liang, J.; Ding, Y.; Xue, G.; Liu, L. Effect of heat treatment on far infrared emission properties of tourmaline powders modified with a rare earth. *Journal of the American Ceramic Society* **2008,** *91* (8), 2588-2592.
(2) Meng, J.; Jin, W.; Liang, J.; Ding, Y.; Gan, K.; Yuan, Y. Effects of particle size on far infrared emission properties of tourmaline superfine powders. *Journal of Nanoscience Nanotechnology* **2010,** *10* (3), 2083-2087.
(3) Guo, C. X.; Zhang, L. Y.; Miao, J.; Zhang, J.; Li, C. M. DNA‐Functionalized Graphene to Guide Growth of Highly Active Pd Nanocrystals as Efficient Electrocatalyst for Direct Formic Acid Fuel Cells. *Advanced Energy Materials* **2013,** *3* (2), 167-171.
(4) Zhang, Y.; Wang, M.; Zhu, E.; Zheng, Y.; Huang, Y.; Huang, X. Seedless growth of palladium nanocrystals with tunable structures: From tetrahedra to nanosheets. *Nano Letters* **2015,** *15* (11), 7519-7525.
(5) Xu, D.; Liu, X.; Han, M.; Bao, J. Facile synthesis of ultrathin single-crystalline palladium nanowires with enhanced electrocatalytic activities. *Chemical Communications* **2016,** *52* (88), 12996-12999.
(6) Zhang, X.; Zhu, J.; Tiwary, C. S.; Ma, Z.; Huang, H.; Zhang, J.; Lu, Z.; Huang, W.; Wu, Y. Palladium nanoparticles supported on nitrogen and sulfur dual-doped graphene as highly active electrocatalysts for formic acid and methanol oxidation. *ACS Applied Materials Interfaces* **2016,** *8* (17), 10858-10865.
(7) Lou, M.; Wang, R.; Zhang, J.; Tang, X.; Wang, L.; Guo, Y.; Jia, D.; Shi, H.; Yang, L.; Wang, X. Optimized synthesis of nitrogen and phosphorus dual-doped coal-based carbon fiber supported Pd catalyst with enhanced activities for formic acid electrooxidation. *ACS Applied Materials Interfaces* **2019,** *11* (6), 6431-6441.
(8) Kankla, P.; Limtrakul, J.; Green, M. L.; Chanlek, N.; Luksirikul, P. Electrooxidation of formic acid enhanced by surfactant-free palladium nanocubes on surface modified graphene catalyst. *Applied Surface Science* **2019,** *471*, 176-184.
(9) Lou, M.; Wang, R.; Yang, L.; Jia, D.; Sun, Z.; Wang, L.; Guo, Y.; Wang, X.; Zhang, J.; Shi, H. Ionic liquid polyoxometalate-enhanced Pd/N, P-codoped coal-based carbon fiber catalysts for formic acid electrooxidation. *Applied Surface Science* **2020,** *516*, 146137.
(10) Mazumder, V.; Chi, M.; Mankin, M. N.; Liu, Y.; Metin, O.; Sun, D.; More, K. L.; Sun, S. A facile synthesis of MPd (M= Co, Cu) nanoparticles and their catalysis for formic acid oxidation. *Nano Letters* **2012,** *12* (2), 1102-1106.
(11) Jin, Y.; Zhao, J.; Li, F.; Jia, W.; Liang, D.; Chen, H.; Li, R.; Hu, J.; Ni, J.; Wu, T. Nitrogen-doped graphene supported palladium-nickel nanoparticles with enhanced catalytic performance for formic acid oxidation. *Electrochimica Acta* **2016,** *220*, 83-90.
(12) Yang, L.; Li, G.; Chang, J.; Ge, J.; Liu, C.; Vladimir, F.; Wang, G.; Jin, Z.; Xing, W. Sea urchin-like Aucore@ Pdshell electrocatalysts with high FAOR performance: Coefficient of lattice strain and electrochemical surface area. *Applied Catalysis B: Environmental* **2020,** *260*, 118200.
(13) Lu, X.; Zheng, L.; Zhang, M.; Tang, H.; Li, X.; Liao, S. Synthesis of core-shell structured Ru@ Pd/C catalysts for the electrooxidation of formic acid. *Electrochimica Acta* **2017,** *238*, 194-201.